GLOBAL PRODUCTIVITY

Global biosphere primary productivity changes during the past eight glacial cycles

Ji-Woong Yang[1]*†, Margaux Brandon[1,2]‡, Amaëlle Landais[1], Stéphanie Duchamp-Alphonse[2], Thomas Blunier[3], Frédéric Prié[1], Thomas Extier[1]§

Global biosphere productivity is the largest uptake flux of atmospheric carbon dioxide (CO_2), and it plays an important role in past and future carbon cycles. However, global estimation of biosphere productivity remains a challenge. Using the ancient air enclosed in polar ice cores, we present the first 800,000-year record of triple isotopic ratios of atmospheric oxygen, which reflects past global biosphere productivity. We observe that global biosphere productivity in the past eight glacial intervals was lower than that in the preindustrial era and that, in most cases, it starts to increase millennia before deglaciations. Both variations occur concomitantly with CO_2 changes, implying a dominant control of CO_2 on global biosphere productivity that supports a pervasive negative feedback under the glacial climate.

A tmospheric carbon dioxide (CO_2) is a potent greenhouse gas that, together with orbital changes, is a primary determinant of Earth's global climate. Measurements of the CO_2 mixing ratio of air trapped in ice cores over the past 800 thousand years (ka) reveal clear glacial-interglacial cycles (1, 2) and show a good correlation with global sea-level changes (3). The Southern Ocean (SO) is thought to have played a major role in these CO_2 variations through changes in sea-ice cover, overturning circulation, and biological productivity (4–7), and there is growing evidence that the terrestrial vegetation may be an important contributor as well [e.g., (8)]. Nevertheless, there are periods during which CO_2 concentration decouples from sea level, particularly during full-glacial periods when CO_2 shows relatively stable or slightly rising trends while sea level continues to decline (9, 10).

To explain this CO_2 evolution during full-glacial times, Galbraith and Eggleston (10) hypothesized a negative feedback by which global photosynthesis becomes limited by low atmospheric CO_2 concentrations, prohibiting further CO_2 drawdown. This hypothesis has not been proven yet by observations because the reconstructions of past biosphere produc-tivity are based on geochemical (e.g., organic and inorganic biomarkers) and micropaleontological (e.g., pollen, coccolith, diatoms) data from sediment archives, which provide indirect and only qualitative reconstructions [e.g., (11)]. Furthermore, they sometimes show contrasting changes, making it difficult to estimate global variations. As an example, terrestrial vegetation records (e.g., arboreal pollen fraction) show a drastic decrease during glacial times, whereas phytoplankton indicators (mainly total organic carbon and alkenones) in the Subantarctic Zone (SAZ), a key part of the SO (6, 12), suggest intensified marine productivity.

The above limitations can be alleviated by using measurements of the triple isotope composition (^{16}O, ^{17}O, and ^{18}O) of atmospheric oxygen (O_2), a marker of global gross productivity expressed in O_2 flux (13). The triple isotopic composition of O_2 is primarily affected by O-isotope exchange with CO_2 during photochemical reactions in the stratosphere and biological reactions of photosynthesis and respiration (13, 14). The heavy isotopes (^{17}O and ^{18}O) are discriminated relative to the light one (^{16}O) in a mass-dependent way during most biological reactions. On the contrary, O_2-CO_2 isotope exchange in the stratosphere fractionates in a mass-independent manner (13–15). Accordingly, to estimate the relative contribution of biosphere and stratosphere fluxes, the ^{17}O anomaly of O_2 is defined as $^{17}\Delta \equiv \ln(\delta^{17}O + 1) - \lambda_{ref}\cdot\ln(\delta^{18}O + 1)$ (16), where λ_{ref} is the mass-dependent reference slope of 0.516 calculated from the modern O_2 isotope fractionations within the global biospheric cycle (16, 17). By definition, tropospheric $^{17}\Delta$ is not modified much by the mass-dependent fractionation within the biosphere. Closed terrarium experiments showed that without stratospheric exchange, biospheric processes induce a positive $^{17}\Delta$ signal relative to that of the present atmosphere (13). By contrast, the stratospheric air measurements from rocket (15), aircraft [e.g., (18, 19)], and balloons [e.g., (19, 20)] showed a highly positive $^{17}\Delta$ of CO_2 as a result of photolysis of O_2 and ozone (O_3) and atomic O exchange with CO_2 (21), which is counterbalanced by a slight depletion of $^{17}\Delta$ of the O_2 reservoir in the stratosphere ($^{17}\Delta_{strat}$) because of the small abundance (mixing ratio) of O_3 relative to O_2 (22). In the present atmosphere, the input of positively fractionated $^{17}\Delta$ from the biosphere ($^{17}\Delta_{bio}$) is equilibrated by a massive flux of O_2 with slightly negative $^{17}\Delta$ from the stratosphere. The sizes of the two endmember fluxes from the biosphere and the stratosphere hence drive the $^{17}\Delta$ variations, so by knowing the magnitudes of the O_2 isotopic fractionations in the stratosphere and O_2 fluxes from the stratosphere (F_{strat}), $^{17}\Delta$ can be used to reconstruct the gross O_2 flux from Earth's biosphere (F_{bio}), or global gross primary productivity in terms of O_2 (GPP-O_2).

The stratosphere influences tropospheric $^{17}\Delta$ through different factors, including F_{strat}, stratosphere temperature, photochemical reaction rates, and O_3 abundance in the stratosphere. Numerical simulations show that greenhouse gases (predominantly CO_2) play an important role in controlling the abovementioned changes in the stratosphere [e.g., (23–26)], allowing the stratosphere effect to be scaled to CO_2 changes such that a high CO_2 mixing ratio in the troposphere induces a strong depletion in $^{17}\Delta$ [see (27) for more details]. It should be noted that O_2 photolysis in the mesosphere may cause additional fractionation (28). However, model simulations suggest that the entrainment of mesospheric air into the stratosphere is small (~0.02%) (28), and its effect on the tropospheric $^{17}\Delta$ is expected to be negligible (27).

As a consequence, the imprint of the stratospheric mass-independent fractionation is reflected in the general anticorrelation between CO_2 and $^{17}\Delta$. However, CO_2 and $^{17}\Delta$ are not always anticorrelated because they decouple when changes in biosphere productivity occur. For example, Brandon et al. (8) pointed out that the notable decoupling over the Termination V (TV)–Marine Isotope Stage (MIS) 11 interval may be interpreted as an imprint of exceptionally high biosphere productivity. Therefore, the decoupling between CO_2 and $^{17}\Delta$ is the key to inferring the past evolution of global biosphere productivity, which provides distinctive insights into the past global carbon cycle.

The previous ice-core record of $^{17}\Delta$ extends over the past 444.8 ka (8, 29). During the past four glacial cycles, which were characterized by a large glacial-interglacial amplitude and a periodicity of ~100 ka, the inferred global

[1]Laboratoire des Sciences du Climat et de l'Environnement/Institut Pierre-Simon Laplace, Université Paris Saclay/CEA/CNRS/UVSQ, Gif-sur-Yvette, France. [2]Géosciences Paris-Saclay, Université Paris Saclay, Orsay, France. [3]Niels Bohr Institute, University of Copenhagen, København N, Denmark.
*Corresponding author. Email: ji-woong.yang@lsce.ipsl.fr
†Present address: Niels Bohr Institute, University of Copenhagen, København N, Denmark.
‡Present address: Laboratoire d'Océanographie et du Climat/Institut Pierre-Simon Laplace, Sorbonne Université/CNRS/IRD/MNHN, Paris, France.
§Present address: Environnements et Paléoenvironnements Océaniques et Continentaux, Université de Bordeaux/CNRS/EPHE, Pessac, France.
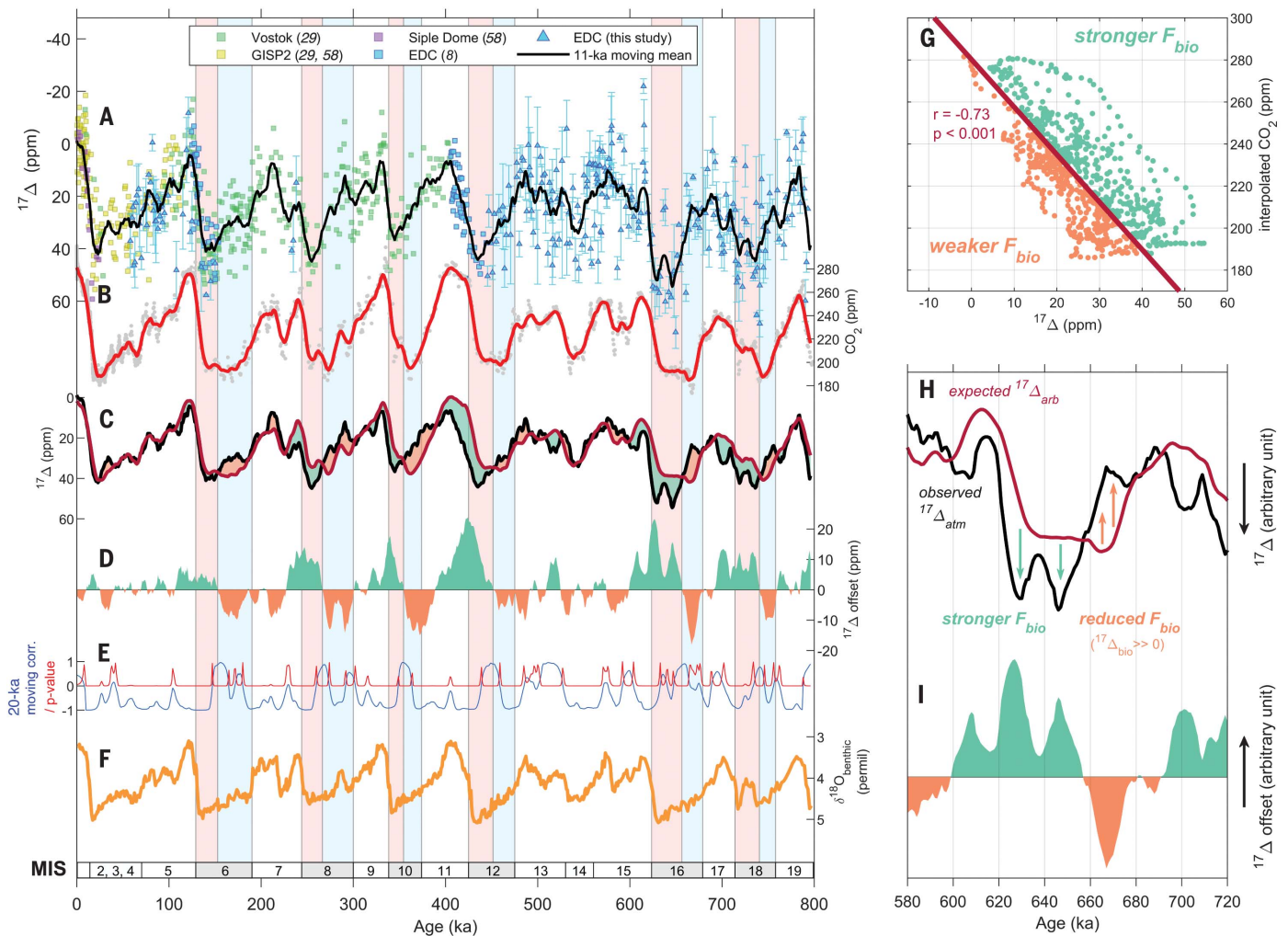
Fig. 1. The 800-ka ice-core composite of $^{17}\Delta$ records. (**A**) Compilation of $^{17}\Delta$ values for multiple ice-core records with previously published data (*8, 29, 58*). The new EDC data produced in this study are plotted in blue triangles with 1σ uncertainty ranges. The smoothed curve of the compilation record is shown as a solid black line. (**B**) Ice-core CO_2 compilation (gray dots) and the smoothed curve (red) (*1, 2*). (**C**) Smoothed $^{17}\Delta$ (black) and $^{17}\Delta_{arb}$ time series (red). (**D**) $^{17}\Delta$ offset between the two time series in (C). (**E**) The 20-ka moving correlation coefficient (blue) and *p* values (red) between the smoothed $^{17}\Delta$ and $^{17}\Delta_{arb}$ time series in (C). (**F**) LR04 benthic $\delta^{18}O$ stack (*59*). The blue and red shadings denote the negative and positive offsets, respectively, during glacial periods within the even-numbered MIS stages as defined by (*59*). permil, parts per thousand. (**G**) Scatter plot of $^{17}\Delta$ and CO_2, both smoothed by an 11-ka moving average (fig. S2). The CO_2 composite data in (B) are interpolated to the ages of the $^{17}\Delta$ data. The linear regression of CO_2 to $^{17}\Delta_{arb}$ is shown in dark red. At given CO_2 concentrations, scatter points to the right (green) and left (orange) of the regression line imply enhanced and reduced F_{bio}, respectively. (**H** and **I**) The enlarged view of (C) and (D) over the MIS 16 interval. All of the plots are based on, or transferred to, Antarctic ice core chronology (AICC) 2012 (*27, 60, 61*). GISP2, Greenland Ice Sheet Project 2.

biosphere productivity was systematically lower during glacial than during interglacial times (*29*). The amplitude of temperature and CO_2 changes over glacial-interglacial transitions was smaller before 450 ka and the glacial periods were shorter than after 450 ka (*2*). Knowing the global biosphere productivity over the period of 800 to 450 ka is hence of uttermost importance to studying the interactions between Earth's biosphere and CO_2 level during the glacial-interglacial cycles. Here, we extend the $^{17}\Delta$ records back to ~796 ka by analyzing samples from the European Project for Ice Coring in Antarctica Dome C (EDC) ice core (*27*). The data were corrected for the

fractionations by gas loss during ice storage, gravitational settling, and bubble close-off (*27*).

Decoupling between $^{17}\Delta$ and CO_2

The fully corrected EDC $^{17}\Delta$ data are plotted with CO_2 in Fig. 1. We observe a general anti-correlation between CO_2 and $^{17}\Delta$ over the past 796 ka [correlation coefficient (*r*) = −0.73; Fig. 1G and fig. S2]. However, this anticorrelation does not hold true during glacial intervals (Fig. 1, A to C): The moving correlation coefficients between CO_2 and $^{17}\Delta$ show a significant positive correlation in the middle of the glacial intervals of MISs 6, 8, 10, 12, 16, and 18 (Fig. 1E). Indeed, CO_2 concentrations show

stable or slightly increasing trends, whereas $^{17}\Delta$ signals gradually increase to glacial maxima (Fig. 1C). We illustrate this decoupling between $^{17}\Delta$ and CO_2 through the $^{17}\Delta$ offset (Fig. 1D), which is the difference between the ice-core $^{17}\Delta$ and a hypothetical $^{17}\Delta$ ($^{17}\Delta_{arb}$) purely driven by stratospheric fractionation (Fig. 1C and fig. S3) (*30*). Negative $^{17}\Delta$ offsets (orange in Fig. 1, D, G, and I) result from reduced biosphere productivity, whereas positive ones (green in Fig. 1, D, G, and I) can be explained by enhanced biosphere productivity. The negative offsets (reduced productivity) are found at earlier stages of glacial periods, whereas the positive ones (increased
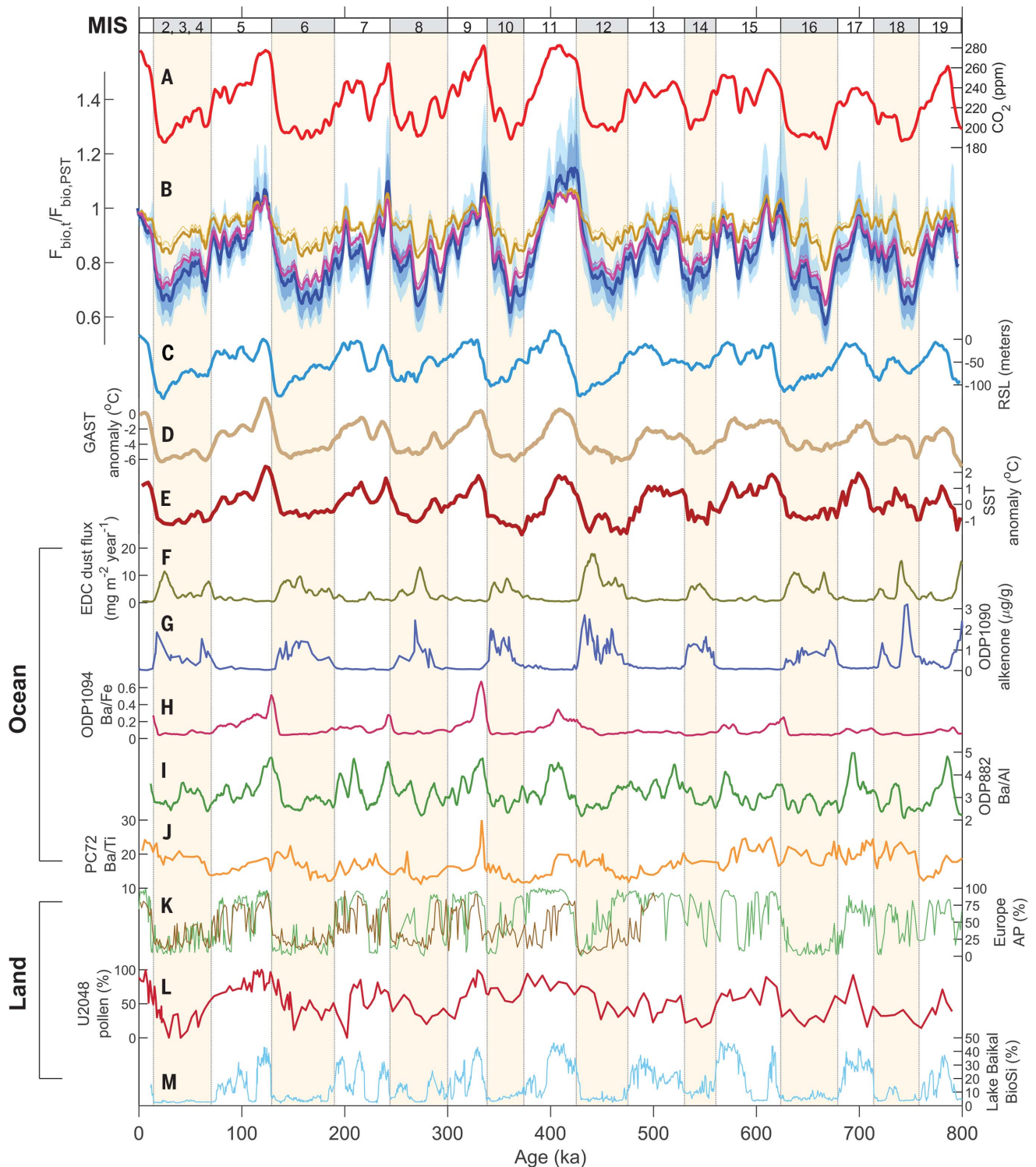
Fig. 2. Comparison of the reconstructed GPP-O$_2$ with global and regional paleoclimate records. (**A**) Ice-core CO$_2$ composite (1, 2) smoothed by a 5-ka moving average. (**B**) GPP-O$_2$ reconstructed by the AL (blue) and TB (pink and yellow) models. For the AL model, the dark and light blue shadings represent 68 and 95% ranges of Monte-Carlo sensitivity solutions, respectively (27). The TB model solutions for a LGM C4 plant contribution of 0.7 (pink) and 0.4 (yellow) are plotted with corresponding curves with the Holocene-LGM ^{17}O anomaly offset of 10 ppm (thin pink and thin yellow lines, respectively). All of the model reconstructions are smoothed by a 5-ka moving average. (**C**) RSL reconstruction (53).

(**D**) GAST anomaly from present (0 to 5 ka) (52). (**E**) Global SST stack (9). (**F**) EDC dust flux (62) smoothed by a 5-ka moving mean. (**G**) Alkenone concentration from the ODP 1090 core (6). (**H**) Ba/Fe ratio from the ODP 1094 core (18) smoothed by a 5-ka moving average. (**I**) Ba/Al ratio at the ODP 882 site (33) smoothed by a 5-ka moving average. (**J**) Ba/Ti ratio from the TT013-PC72 core (34). (**K**) Arboreal pollen (AP) fraction from Lake Ohrid (brown) (41) and Tenaghi Philippon (dark green) (40). (**L**) Fractional abundances of the pollen end-members at the MD96-2048 core, southeastern Africa (42). (**M**) Biogenic silica from Lake Baikal (43). Yellow shadings indicate the glacial periods.
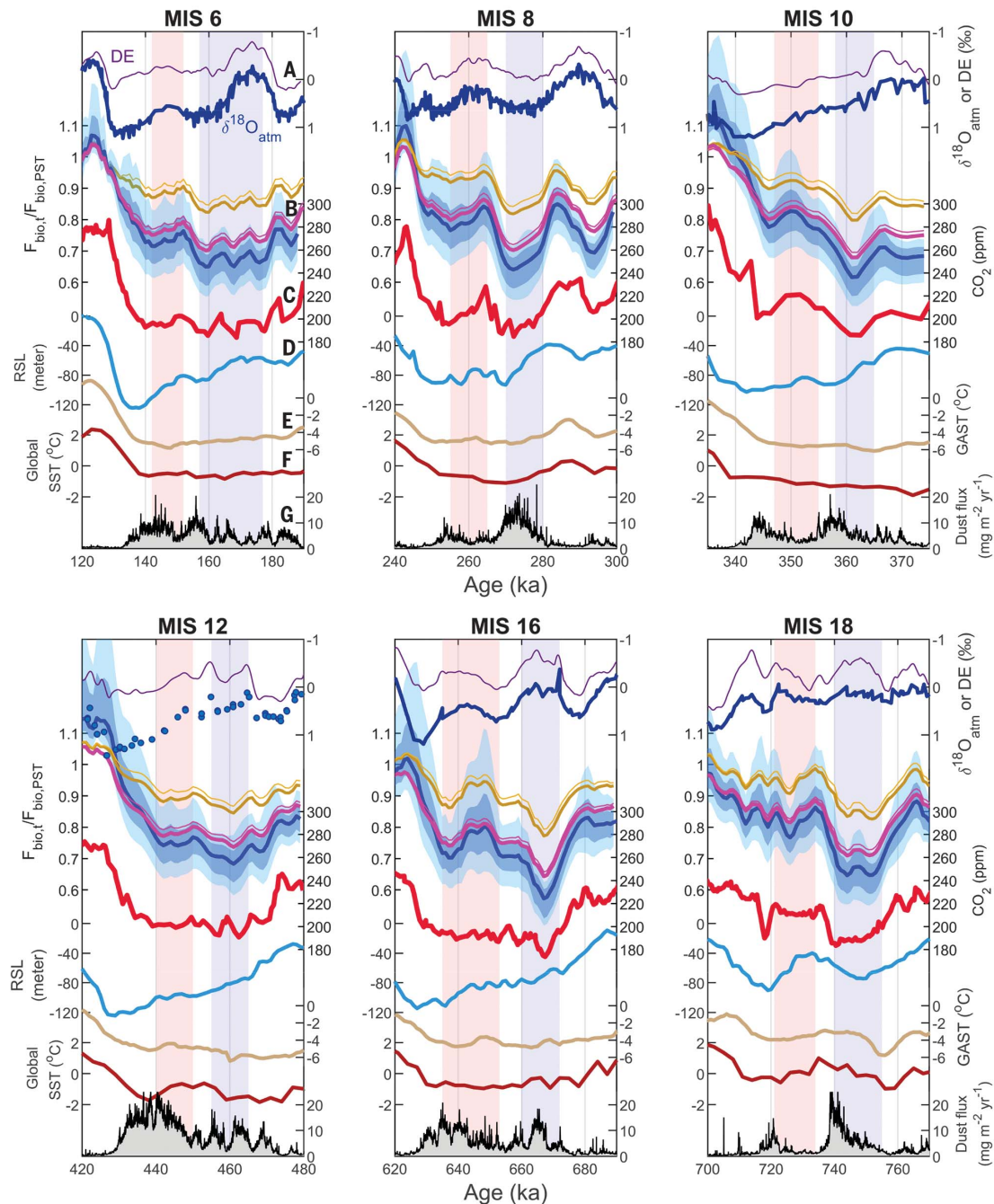
Fig. 3. Close-up of GPP-O_2 evolution during glacial intervals with different climate proxies. (**A**) Ice-core $\delta^{18}O_{atm}$ composite (dark blue) (63) and DE (purple) (56). (**B**) GPP-O_2 reconstructions using the AL and TB models in the same color schemes as in Fig. 2. (**C**) Ice-core CO_2 composite (1, 2). (**D**) RSL reconstruction (53). (**E**) GAST anomaly from present (0 to 5 ka) (52). (**F**) Global SST stack (9). (**G**) EDC dust flux (62). Blue and red shadings indicate the mid- and full-glacial stages, respectively.

productivity) prevail from later stages of glacial to interglacial periods.

GPP-O_2 reconstructions using box models

To obtain a more quantitative assessment of past changes in global biosphere productivity, we applied two different box models [the T. Blunier (TB) (29) and A. Landais (AL) models (31)] that describe triple O_2 isotope budgets in the biosphere, troposphere, and stratosphere. Assuming steady state, both models calculate the biosphere O_2 flux so that the biosphere input of $^{17}\Delta$ is balanced by O_2 flux

from the stratosphere, which is estimated from the CO_2 concentration in the troposphere (13). The different assumptions made by the two models and their limitations are described in the supplementary materials (27).

The reconstructed GPP-O_2 from the two different models are presented in Fig. 2B in terms of the ratio between the global biosphere O_2 flux of the past ($F_{bio,t}$) and the global biosphere O_2 flux of the preindustrial condition ($F_{bio,PST}$). Although the two model results are not necessarily identical, they share common features

that confirm our qualitative inferences based on $^{17}\Delta$ offset (Fig. 1): (i) They reveal clear glacial (low productivity)–interglacial (high productivity) cycles during the past 796 ka, (ii) the GPP-O_2 minima during each glacial period occurred under intermediate sea level and concomitantly with glacial CO_2 minima (mid-glacial stage) (Fig. 2, A and B), and (iii) following the glacial minima, GPP-O_2 increases while global ice volume continues to grow until the glacial maxima (full-glacial stage), millennia before the glacial terminations (Figs. 2B and 3B).
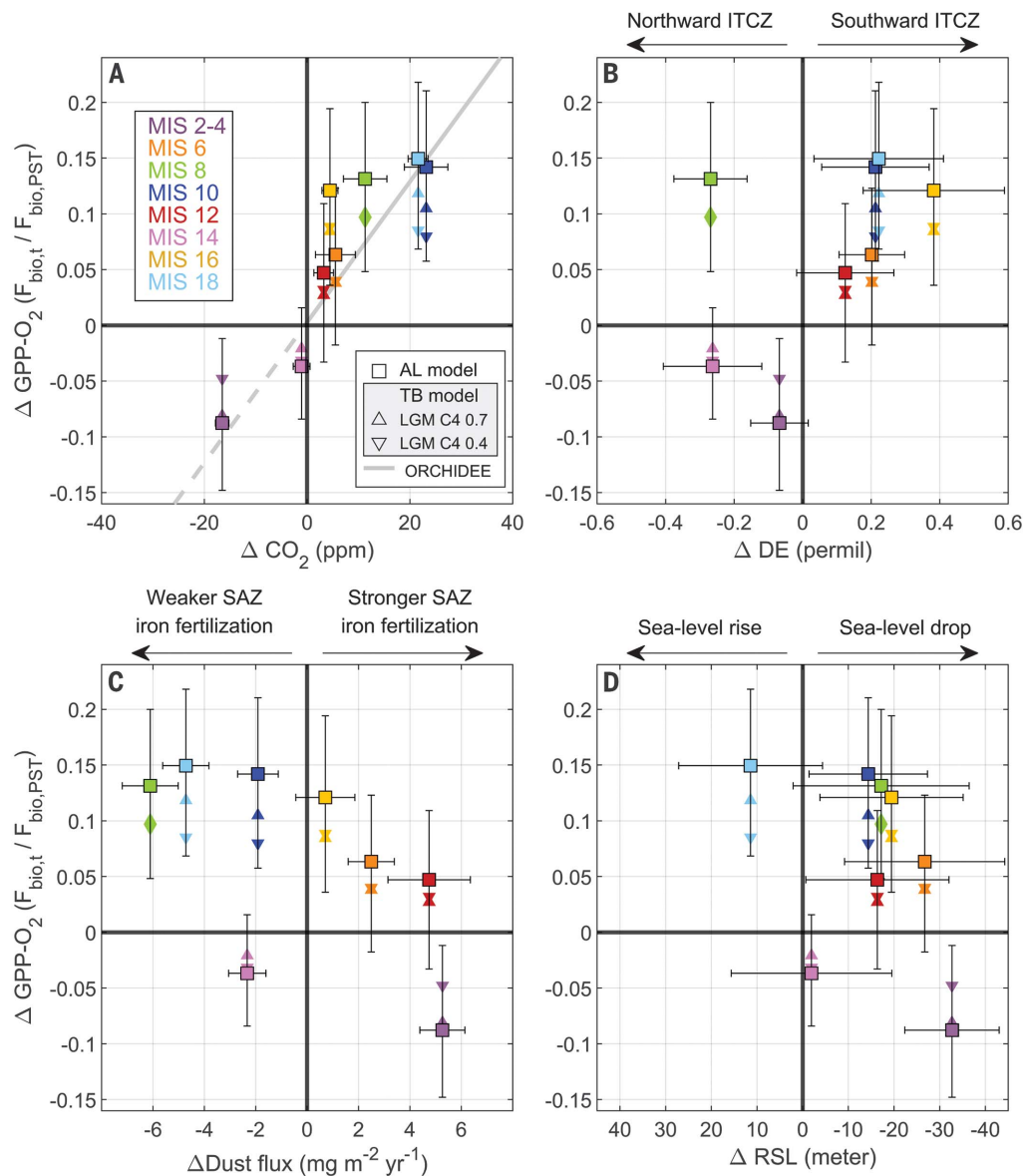
Fig. 4. Comparison of the magnitude of changes in GPP-O$_2$ and potential climatic controls between the two glacial stages. The differences (expressed in Δ) between the average values of the two stages (full-glacial minus mid-glacial stages) as defined in Fig. 3. Both ΔGPP-O$_2$ results from the AL (square) and TB (triangle) models are plotted. (**A**) Comparison with CO$_2$ changes. The solid gray line stands for the ΔGPP-O$_2$ predicted by second-order regression of CO$_2$-sensitivity simulations using the ORCHIDEE model (44), assuming constant ocean productivity and terrestrial-to-marine GPP ratio. The ΔGPP-O$_2$ uncertainties are taken as 16 to 84 percentiles of the Monte-Carlo simulations ($n = 1000$) of 26 sensitivity scenarios. CO$_2$ uncertainties are taken from (2). (**B**) Comparison with DE changes (56). The positive changes indicate southward displacement of the tropical rainbelt. The uncertainties for ΔDE are based on the 1σ errors reported in (56). (**C**) Comparison with changes in EDC dust flux (62). The positive offset implies stronger iron fertilization in the SO during full-glacial stages compared with mid-glacial stages. ΔDust flux uncertainty is estimated by assuming the maximum analytical error reported as 10% (62). (**D**) Comparison with RSL changes (53). The ΔRSL uncertainty is based on the 1σ uncertainty ranges in (53).

Glacial-interglacial changes

Both box-model results indicate concomitant GPP-O$_2$ and CO$_2$ minima during each of the eight glacial intervals (Fig. 2), with glacial productivity minima that are estimated to lie between 55 and 87% of modern productivity. In the following sections, we explore the possible contributions of marine and terrestrial productivity to this large reduction of global GPP-O$_2$ under glacial times.

The only global compilation of marine sedimentary records of marine productivity that exist for glacial times focuses on the Last Glacial Maximum (LGM) and indicates stronger export production and probably higher marine primary productivity (PP) during the LGM than during the Holocene (12). Over the past 800 ka, the very few available marine export production records that are suggested

to reflect PP reveal spatially different patterns during glacial times. The alkenone concentration at the Ocean Drilling Program (ODP) 1090 site located in the SAZ shows an increased PP during glacial periods (6), whereas biogenic barium (Ba/Fe) from ODP 1094 in the Antarctic Zone of the SO (32) and the Ba/Al ratio from the ODP 882 core in the subarctic Pacific (33) indicate reduced PP (Fig. 2, G to I). In addition, the Ba/Ti record from the core TT013-PC72 in the Equatorial Pacific exhibits no clear glacial-interglacial pattern (34) (Fig. 2J). None of those records explain our reconstructed lower global GPP-O$_2$ during glacial periods. Global ocean PP in glacial times is difficult to predict, and ocean biogeochemical models have shown contrasting results: Some predict greater global PP in the LGM (35), whereas others represent the opposite (36)

or no clear change (37). On the one hand, a decrease in ocean PP is expected because colder sea surface temperature (SST) reduces the metabolic rate of marine phytoplankton [e.g., (38)], shoaling of overturning circulation reduces the intake of nutrient-rich deep water (39), and highly productive continental shelf areas are lost by sea-level decline. On the other hand, an increase in ocean PP could arise from greatly enhanced aeolian dust deposition that supplies iron to high-nutrient low-chlorophyll oceans such as the SO [e.g., (6)].

No direct proxies for terrestrial GPP exist, but we do have indirect vegetation cover proxies, some of which reflect glacial shrinking and interglacial expansion patterns. Two long-term pollen assembly records in Europe—Tenaghi Philippon (40) and Lake Ohrid (41)—clearly indicate a near vanishing arboreal-type pollen

during glacial periods (Fig. 2K). In addition, woodland- and mountain forest–type vegetations from the MD96-2048 core off southeastern Africa exhibit glacial-interglacial variations (42) (Fig. 2L). Similar glacial-interglacial patterns are observed in biogenic silica records from the BDP-96 core from Lake Baikal (43) (Fig. 2M).

Several arguments favor a stronger decrease in terrestrial GPP than in marine PP during glacial intervals. A nearly 90 parts per million (ppm) lower concentration of CO_2 in the glacial atmosphere would have a strong negative fertilizing effect on photosynthesis of terrestrial vegetation (44, 45), whereas its impact on marine PP is expected to be minor (46). A modeling study using a dynamic global vegetation model (DGVM) shows that with a CO_2 increase of 185 to 285 ppm, the vegetation GPP increases by more than a factor of two GPP (44). The effects of temperature and precipitation on terrestrial GPP are less clear. Although modern observations suggest that temperature and precipitation are important controls for terrestrial GPP [e.g., (47)], model studies show that climate change alone (without changes in CO_2) has a limited impact on glacial-interglacial vegetation GPP changes (45, 48). A glacial sea-level low stand might have two opposing effects, with the exposure of continental shelves promoting increased amounts of new vegetation (49, 50) and ice-sheet expansion prohibiting photosynthesis in the ice-covered area. Previous DGVM simulations suggested that the relative sea-level (RSL) decline would increase LGM vegetation net primary productivity (NPP) by ~8% relative to constant RSL results (51). Taken together, it is therefore likely that the glacial-interglacial changes in global GPP-O_2 are largely driven by terrestrial productivity, whose evolution is strongly influenced by CO_2.

Glacial productivity changes

The glacial productivity minima occur at mid-glacial stages, followed by the systematic increase in GPP-O_2 from mid- to full-glacial stages. Such an increase in productivity between mid- and full-glacial stages is not easy to detect from paleoproductivity proxies because of a lack of high-resolution records and/or chronological issues. In the ocean, neither ODP 1090 alkenone concentrations nor ODP 882 Ba/Al records exhibit a detectable shift between the two stages, with the exceptions of MISs 6 and 12 (ODP 1090) and MIS 8 (ODP 882) (Fig. 2, G and I). In parallel, the TT-13-PC72 Ba/Ti record starts to rise several millennia before maximum productivity at deglacial terminations (Fig. 2J). In the terrestrial realm, the arboreal pollen fractions at Tenaghi Phillippon and Lake Ohrid and biogenic silica at Lake Baikal indicate nearly vanished productivity during glacial times, showing no clear trends during the mid- to full-glacial changes (Fig. 2,

K and M). By contrast, the MD96-2048 pollen assemblage records show that the fractions of woodland and mountain forest species increased in the late-glacial stages during certain glacial intervals such as MISs 6, 8, 10, and 12 (Fig. 2L). Therefore, despite the complexity of comparing our GPP-O_2 records with local records, the GPP-O_2 increase between mid- and full-glacial stages is confirmed by some local records.

There are several ways in which the possible contributions of the main potential drivers of GPP-O_2 might help to explain the increasing GPP-O_2 signal between full- and mid-glacial stages. As mentioned previously, the CO_2 fertilization effect may play a major role, and there is a clear correlation between GPP-O_2 and CO_2 changes over the mid- to full-glacial stages (Fig. 4). The observed GPP-O_2 versus CO_2 changes agree with a second-order fitting of Chen et al.'s (44) sensitivity simulations (Fig. 4A). However, over MISs 8 and 16, the GPP-O_2 versus CO_2 relationship is slightly different, suggesting that factors other than CO_2 concentration affect the GPP-O_2 evolution during glacial periods (Fig. 4A).

First, the global temperature change between mid- and full-glacial stages is minor. The global air surface temperature (GAST) reconstructions (52) and a global SST stack (9) show no warming or only limited changes (Fig. 3).

Second, RSL reconstructions indicate sea-level declines of 10 to 30 m between mid- and full-glacial stages in most glacial periods (53) (Fig. 3). Recalling that there was an ~8% increase in terrestrial NPP at the LGM for an RSL change of ~120 m (51, 53), the sea-level decline between two glacial stages should have only a small effect. Moreover, the comparison between GPP-O_2 and RSL records shows no strong relationship (Fig. 4D). Therefore, we suggest that the sea-level changes have a minor impact on glacial GPP-O_2 changes.

Third, low-latitude hydrological changes could play a role as well, because global vegetation is expected to be shifted southerly during glacial periods owing to Northern Hemisphere ice-sheet expansion [e.g., (54)]. Climate model experiments for the LGM show an increase in precipitation in Southern Hemisphere low-latitude regions, such as Amazonia and South Africa, for which modeled vegetation NPP is increased in tropical and temperate forests as compared to present (45). Proxies for past evolution of the low-latitude water cycle exist, such as the Dole effect (DE), that is, the $\delta^{18}O$ offset between air O_2 and sea water (14), and speleothem $\delta^{18}O_{calcite}$ from Chinese caves (55). The long DE records (56) indicate a mid- to full-glacial enrichment over most glacial periods when GPP-O_2 increases, which implies a further southward shift of the Intertropical Convergence Zone (ITCZ) from

mid- to full-glacial stages (Fig. 4B). This is supported by $\delta^{18}O_{calcite}$ records from Chinese caves over MISs 6 and 10 (55). Therefore, this evidence suggests that a southward shift of the ITCZ at the full-glacial stages might have stimulated terrestrial GPP-O_2.

Finally, marine productivity may also contribute to this GPP-O_2 increase, especially in the SO, where PP is usually limited by iron [e.g., (57)]. This iron limitation is alleviated by greater dust deposition into the SAZ, which is caused by stronger winds, together with glacial aridity and the meridional shift of westerly winds (6). However, the changes in EDC dust flux are not systematically positively correlated with GPP-O_2 increases (Fig. 4C): The full-glacial increases in EDC dust flux are observed only in MISs 6, 12, and 16, where the GPP-O_2 increases are relatively small (Fig. 4C).

Summary

Our $^{17}\Delta$ data provide a complete view of global biosphere productivity evolution during the past 800 ka, which confirms the pervasive glacial (low GPP)–interglacial (high GPP) cycles, and demonstrate an important feature of intraglacial GPP shift. The GPP reconstructions and proxy evidence discussed here suggest that much of the GPP-O_2 changes over glacial-interglacial cycles and between two glacial stages are dominantly attributable to CO_2 changes and that, in both cases, terrestrial GPP might have played an important role. Our findings also demonstrate the close interactions of global photosynthesis with CO_2 over the past 800 ka, providing observational evidence of the pervasive negative feedback between global photosynthesis and CO_2 (10).

REFERENCES AND NOTES

1. D. Lüthi et al., Nature 453, 379–382 (2008).
2. B. Bereiter et al., Geophys. Res. Lett. 42, 542–549 (2015).
3. G. L. Foster, E. J. Rohling, Proc. Natl. Acad. Sci. U.S.A. 110, 1209–1214 (2013).
4. B. B. Stephens, R. F. Keeling, Nature 404, 171–174 (2000).
5. D. M. Sigman, M. P. Hain, G. H. Haug, Nature 466, 47–55 (2010).
6. A. Martínez-Garcia et al., Paleoceanography 24, PA1207 (2009).
7. S. Duchamp-Alphonse et al., Nat. Commun. 9, 2396 (2018).
8. M. Brandon et al., Nat. Commun. 11, 2112 (2020).
9. J. D. Shakun, D. W. Lea, L. E. Lisiecki, M. E. Raymo, Earth Planet. Sci. Lett. 426, 58–68 (2015).
10. E. D. Galbraith, S. Eggleston, Nat. Geosci. 10, 295–298 (2017).
11. K. B. Averyt, A. Paytan, Paleoceanography 19, PA4003 (2004).
12. K. E. Kohfeld, C. Le Quéré, S. P. Harrison, R. F. Anderson, Science 308, 74–78 (2005).
13. B. Luz, E. Barkan, M. L. Bender, M. H. Thiemens, K. A. Boering, Nature 400, 547–550 (1999).
14. M. Bender, T. Sowers, L. Labeyrie, Global Biogeochem. Cycles 8, 363–376 (1994).
15. M. H. Thiemens, T. Jackson, E. C. Jipf, P. W. Erdman, C. van Egmond, Science 270, 969–972 (1995).
16. B. Luz, E. Barkan, Geochim. Cosmochim. Acta 69, 1099–1110 (2005).
17. Recent laboratory incubation studies suggested either a lower λ of ~0.510 (64) or a higher λ of ~0.522 (65) during dark respiration; however, sensitivity tests performed with a λ of 0.510 and 0.520 lead to $^{17}\Delta$ variations within the uncertainty range. See (27) for more details.
18. K. A. Boering et al., Geophys. Res. Lett. 31, L03109 (2004).
19. A. A. Wiegel et al., Proc. Natl. Acad. Sci. U.S.A. 110, 17680–17685 (2013).

20. B. Alexander, M. K. Vollmer, T. Jackson, R. F. Weiss, M. H. Thiemens, *Geophys. Res. Lett.* **28**, 4103–4106 (2001).
21. Y. L. Yung, W. B. DeMore, J. P. Pinto, *Geophys. Res. Lett.* **18**, 13–16 (1991).
22. M. H. Thiemens, M. Lin, *Rev. Mineral. Geochem.* **86**, 35–95 (2021).
23. N. Butchart *et al.*, *Clim. Dyn.* **27**, 727–741 (2006).
24. K. P. Shine *et al.*, *Q. J. R. Meteorol. Soc.* **129**, 1565–1588 (2003).
25. G. Chiodo *et al.*, *J. Clim.* **31**, 3893–3907 (2018).
26. E. L. Fleming, C. H. Jackman, R. S. Stolarski, A. R. Douglas, *Atmos. Chem. Phys.* **11**, 8515–8541 (2011).
27. Materials and methods are available as supplementary materials.
28. M.-C. Liang, G. A. Blake, B. R. Lewis, Y. L. Yung, *Proc. Natl. Acad. Sci. U.S.A.* **104**, 21–25 (2007).
29. T. Blunier, M. L. Bender, B. Barnett, J. C. von Fischer, *Clim. Past* **8**, 1509–1526 (2012).
30. $^{17}\Delta_{arb}$ is the expected $^{17}\Delta$ in the troposphere if the biosphere (F_{bio} and $^{17}\Delta_{bio}$) remains constant over time; hence, it is hypothesized to be affected by the stratosphere only. The stratosphere changes are assumed to be limited by CO_2 (*13*, *31*). $^{17}\Delta_{arb}$ is therefore calculated as tropospheric $^{17}\Delta$ in the steady-state equations S2 and S4 in the three-box model (AL model) by assuming constant F_{bio} and $^{17}\Delta_{bio}$ [see (*27*) for more details].
31. A. Landais, J. Lathiere, E. Barkan, B. Luz, *Global Biogeochem. Cycles* **21**, GB1025 (2007).
32. S. L. Jaccard *et al.*, *Science* **339**, 1419–1423 (2013).
33. S. L. Jaccard, E. D. Galbraith, D. M. Sigman, G. H. Haug, *Quat. Sci. Rev.* **29**, 206–212 (2010).
34. R. W. Murray, C. Knowlton, M. Leinen, A. C. Mix, C. H. Polsky, *Paleoceanography* **15**, 570–592 (2000).
35. V. Brovkin, A. Ganopolski, D. Archer, S. Rahmstorf, *Paleoceanography* **22**, PA4202 (2007).
36. A. Tagliabue *et al.*, *Clim. Past* **5**, 695–706 (2009).
37. L. Bopp, K. E. Kohfeld, C. Le Quéré, O. Aumont, *Paleoceanography* **18**, 1046 (2003).
38. R. W. Eppley, *Fish Bull.* **70**, 1063 (1972).
39. J. B. Palter, J. L. Sarmiento, A. Gnanadesikan, J. Simeon, R. D. Slater, *Biogeosciences* **7**, 3549–3568 (2010).
40. P. C. Tzedakis, H. Hooghiemstra, H. Pälike, *Quat. Sci. Rev.* **25**, 3416–3430 (2006).
41. L. Sadori *et al.*, *Biogeosciences* **13**, 1423–1437 (2016).
42. L. M. Dupont, T. Caley, I. S. Castaneda, *Clim. Past* **15**, 1083–1097 (2019).
43. A. A. Prokopenko, L. A. Hinnov, D. F. Williams, M. I. Kuzmin, *Quat. Sci. Rev.* **25**, 3431–3457 (2006).
44. W. Chen *et al.*, *Quat. Sci. Rev.* **218**, 293–305 (2019).
45. M. N. Woillez *et al.*, *Clim. Past* **7**, 557–577 (2011).
46. M. Hein, K. Sand-Jensen, *Nature* **388**, 526–527 (1997).
47. A. Anav *et al.*, *Rev. Geophys.* **53**, 785–818 (2015).
48. M. Martin Calvo, I. C. Prentice, *New Phytol.* **208**, 987–994 (2015).
49. T. Hanebuth, K. Stattegger, P. M. Grootes, *Science* **288**, 1033–1035 (2000).
50. X. Wang, X. Sun, P. Wang, K. Stattegger, *Palaeogeogr. Palaeoclimatol. Palaeoecol.* **278**, 88–97 (2009).
51. B. A. A. Hoogakker *et al.*, *Clim. Past* **12**, 51–73 (2016).
52. C. W. Snyder, *Nature* **538**, 226–228 (2016).
53. R. M. Spratt, L. E. Lisiecki, *Clim. Past* **12**, 1079–1092 (2016).
54. I. C. Prentice, S. P. Harrison, P. J. Bartlein, *New Phytol.* **189**, 988–998 (2011).
55. H. Cheng *et al.*, *Nature* **534**, 640–646 (2016).
56. E. Huang *et al.*, *Sci. Adv.* **6**, eaba4823 (2020).
57. M. P. Hain, D. M. Sigman, G. H. Haug, in *Treatise on Geochemistry, Volume 8: The Oceans and Marine Geochemistry*, H. D. Holland, K. K. Turekian, Eds. (Elsevier, ed. 2, 2014), pp. 485–517.
58. T. Blunier, B. Barnett, M. L. Bender, M. B. Hendricks, *Global Biogeochem. Cycles* **16**, 1029 (2002).
59. L. E. Lisiecki, M. E. Raymo, *Paleoceanography* **20**, PA1003 (2005).
60. L. Bazin *et al.*, *Clim. Past* **9**, 1715–1731 (2013).
61. D. Veres *et al.*, *Clim. Past* **9**, 1733–1748 (2013).
62. F. Lambert, M. Bigler, J. P. Steffensen, M. Hutterli, H. Fischer, *Clim. Past* **8**, 609–623 (2012).
63. T. Extier *et al.*, *Quat. Sci. Rev.* **185**, 244–257 (2018).
64. J. L. Ash, H. Hu, L. Y. Yeung, *ACS Earth Space Chem.* **4**, 50–66 (2020).
65. D. A. Stolper, W. W. Fischer, M. L. Bender, *Geochim. Cosmochim. Acta* **240**, 152–172 (2018).
66. J.-W. Yang *et al.*, Triple isotopic composition of atmospheric oxygen (Δ17O of O2) over 58.0-150.0, 233.2-238.1, and 445.6-796.3 ka from EPICA Dome C ice core. PANGAEA (2022); https://doi.org/10.1594/PANGAEA.941483.

ACKNOWLEDGMENTS

SUPPLEMENTARY MATERIALS